Journal of Materials Chemistry C

PAPER

View Article Online
View Journal | View Issue

Cite this: J. Mater. Chem. C, 2016, 4, 1313

Enhanced thermoelectric properties of Au nanodot-included Bi_2Te_3 nanotube composites

Eunsil Lee,[a] Jieun Ko,[a] Jong-Young Kim,*[a] Won-Seon Seo,[b] Soon-Mok Choi,[c] Kyu Hyoung Lee,*[d] Wooyoung Shim[e] and Wooyoung Lee[e]

Received 23rd November 2015,
Accepted 11th January 2016

DOI: 10.1039/c5tc03934g

www.rsc.org/MaterialsC

Herein, we report on a scalable synthesis of Au nanodot (Au-ND)/Bi_2Te_3 nanotube (BT-NT) nanocomposites by the bottom-up synthesis of hybrid raw materials and subsequent spark plasma sintering, and their thermoelectric properties were systematically compared with those of Au-doped Bi_2Te_3 compounds. The Au nanodots were included as seeds and co-crystallized in the crystal growth of BT-NTs, which were well-dispersed in the Bi_2Te_3 matrix as nanoinclusions (10–20 nm). The thermoelectric performance (*ZT*) of the Au-ND/BT-NT nanocomposite was found to be enhanced by ~67%, compared to pristine Bi_2Te_3 due to electron energy filtering and phonon scattering effects in the presence of embedded Au-NDs. The resulting compound showed an enhanced power factor (23.0 × 10^{-4} W m^{-1} K^{-2} @ 440 K, 27% improvement) and a reduced lattice thermal conductivity (0.47 W m^{-1} K^{-1} @ 440 K, 22% reduction). The peak *ZT* value of the present compound (0.95 @ 480 K) is larger than that of n-type single crystalline $Bi_2(Te,Se)_3$, which is one of the highest among the reported values for n-type Bi_2Te_3-based materials synthesized using a soft chemical route.

1. Introduction

Thermoelectric power generation (TEG) is a core technology for renewable energy harvesting and greenhouse gas reduction. For the extensive use of TEG systems, it is essential to enhance the performance of thermoelectric (TE) materials, which can be evaluated by a dimensionless figure of merit $ZT = \sigma S^2 T/\kappa$ (σ is the electrical conductivity, S is the Seebeck coefficient, T is the absolute temperature, and κ is the total thermal conductivity). Bi_2Te_3 (BT)-based solid solutions, such as p-type $Bi_{2-x}Sb_xTe_3$ (BST) and n-type $Bi_2Te_{3-y}Se_y$ (BTS), are considered the best TE materials used at near room temperature. Although BT-based materials are now being used widely for small-scale or high-density cooling systems, materials with a higher *ZT* are required for further extension of their applications, including domestic cooling and power generation from low-grade heat (<100 °C).

The ingots of BT-based alloys are synthesized using a solid-state reaction method, which generally requires high processing temperatures (>1000 K) and a long reaction time. Meanwhile, 2-dimensional nanoplates or 1-D nanowires of TE alloys can be synthesized using a solution-based bottom-up synthesis route at a lower temperature.[1–4] A main advantage of this technique lies in the simplicity and scalability. Additionally, bottom-up synthesis allows better control of nano- and/or hetero-structured materials compared to top-down approaches such as milling or melt spinning. Thus well designed nano-scale structures could be formed in bulk materials. The sintered nanograined bulks of nanoplates or nanowires offer a lower lattice thermal conductivity (κ_{latt}) than those made of ingots due to the intensified phonon scattering at highly-dense grain boundaries.[1–4] A further enhancement of *ZT* in these nanograined bulks could be obtained by an increase of the power factor ($S^2\sigma$) through the modification of the electronic structure. As proposed by Faleev *et al.*[5] and Zebarjadi *et al.*,[6] this can be achieved by introducing metal nanoinclusions in the semiconducting TE matrix, which results in a simultaneous improvement of thermal (reduced κ_{latt}) and electronic (enhanced power factor) transport properties.[7–10] The interfaces between metal nanoinclusions and the TE matrix act as potential barriers[11,12] or potential wells[5] for filtering carriers with low energy levels to induce the scattering of carriers as well as phonon scattering centers. The S enhancement by carrier filtering has been experimentally verified using PbTe and III–V semiconductor materials composed of a thin film superlattice,[13,14] nanograins,[15–17] and nanoinclusions,[18–22] respectively.

According to theoretical considerations, the band bending at the metal–semiconductor (MS) interface forms potential energy

[a] Icheon Branch, Korea Institute of Ceramic Engineering and Technology, Icheon 17303, Korea. E-mail: jykim@kicet.re.kr
[b] Energy and Environmental Division, Korea Institute of Ceramic Engineering and Technology, Jinju 52851, Korea
[c] School of Energy, Materials and Chemical Engineering, Korea University of Technology and Education, Cheonan 31253, Korea
[d] Department of Nano Applied Engineering, Kangwon National University, Chuncheon 24341, Korea. E-mail: khlee2014@kangwon.ac.kr
[e] Department of Materials Science & Engineering, Yonsei University, Seoul 03722, Korea

barriers for blocking low energy carriers. This carrier energy filtering results in an improved S for a given carrier concentration (n) since charges are moved by carriers, which have higher average energy. The power factor can be either increased or decreased depending on the barrier height of the MS interface, which is dependent on the position of a semiconductor fermi level relative to the work function (Φ) of the metal. However, a detailed experimental investigation of the effect of the band alignment on S and σ is still lacking especially for a BT-based hetero-structured system even though elaborated MS junction formation is required to maximize the power factor.

In our previous study, we found two key factors for S enhancement by the carrier filtering effect in nanodot embedded hetero-structured p-type Bi–Sb–Te;[23] the band alignment and the interface density between the TE host Bi–Sb–Te and the nanodot. Thus, we selected Au as the nanodot (Au-ND) because the work function of Au (5.31–5.47 eV)[22] is well suited to electron affinity ($\chi \sim 4.5$ eV)[24] and Φ of BT (5.3 eV),[25,26] and the size of Au-ND could be easily controlled through the alteration of synthesis conditions. A controlled potential barrier (V_B) for energy filtering is expected to be optimal in the power factor enhancement according to the previous theoretical study (Fig. 1a).[5,15] Au-NDs were synthesized using the micro-emulsion method, and co-crystallized in the crystal growth of BT nanotubes (BT-NTs) using a bottom-up synthesis method, which enables us to produce a coherent interface between metallic Au and semi-conducting BT (Fig. 1b). Furthermore, with respect to the Au-ND/BT-NT composite and Au-doped BT, the TE transport properties were compared. The results of this study show that the overall improvement of ZT (>67%) for Au-ND/BT-NT materials is attributable to an enhanced power factor (27%) and reduced κ_{latt} (22%) due to the energy filtering effect in combination with phonon scattering in the presence of Au-ND inclusions.

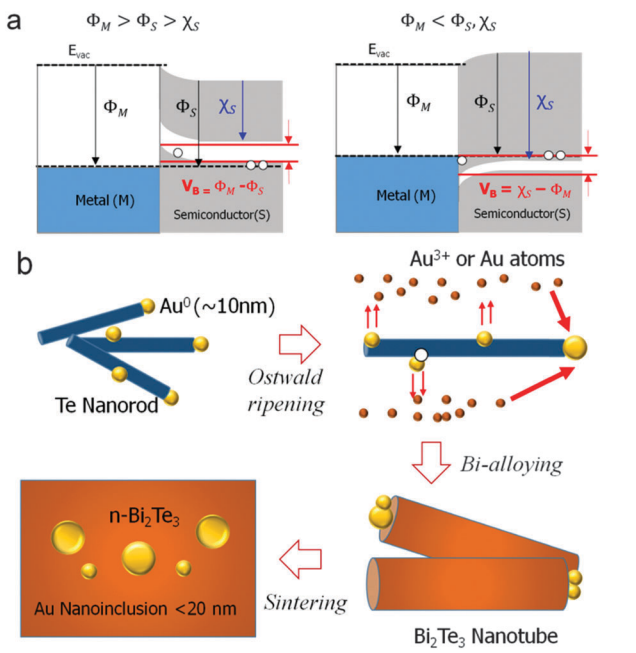

Fig. 1 (a) Band diagrams of metal and semiconductor interfaces. (b) A schematic of Au-nanodot/Bi_2Te_3 nanotube hybrid synthesis.

2. Experiments

2.1. Starting materials

TeO_2 (Alfa Aesar, 99.9995%), NaOH (DaeJung, 98%), polyvinyl-pyrrolidone (PVP, Sigma Aldrich, $M_w \sim 40\,000$), ethyleneglycol (DaeJung, 99.5%), hydrazine monohydrate (Junsei, 98%), bismuth nitrate hydrate (Sigma Aldrich, 99.99%), gold chloride hydrate (Sigma Aldrich, 99.999%), and trisodium citrate dehydrate (Daejung, 99%) were used as received.

2.2. Au nanodot synthesis

Firstly, 0.039 g of gold chloride hydrate was dissolved in 100 mL of distilled water, and heated to 90 °C with stirring. Then, 0.235 g of trisodium citrate dehydrate was dissolved in 20 mL of distilled water and was poured into hot Au solution. The mixed solution was heated for 10 min at 100 °C and the resulting red-black suspension was cooled down to room temperature.

2.3. Au nanodot–Bi_2Te_3 nanotube hybrid synthesis

During the bottom-up synthesis of BT-NTs, aqueous Au-ND solution was added at different proportions, and then reacted in the BT-NT growth process for the formation of a coherent interface between Au-NDs and BT-NTs. The BT-NTs were grown by a two-step solution phase reaction. Te nanorods (Te-NRs) were grown first using Au-nanodots as seeds, and then we perform an alloying reaction to diffuse Bi into the Te-NRs to form the BT-NTs (Fig. 1b). For Te-NRs, 70 mL of ethylene glycol is added to a three-neck flask under a N_2 flowing atmosphere, followed by adding of 1.0 g of PVP, 2.1 g of KOH, and 1.115 g of TeO_2 powder (99.9995%) in the presence of Au-NDs. The mixture is heated to 120 °C with nitrogen protection, and then 2.25 mL of hydrazine monohydrate is added to the above solution as a reducing agent. Uniform Te-NRs are formed in 40 min. Bi precursor solution is made by dissolving 2.265 g of $Bi(NO_3)_3{\cdot}5H_2O$, 0.15 g of PVP, and 2.25 mL of hydrazine monohydrate into 15 mL of ethylene glycol. For BT-NTs, the as-prepared Bi precursor solution is injected into the above Te-NR solution at 120 °C. After another 40 min reaction, hybrid powders of Au-ND/BT-NTs are obtained. The remaining surfactant and reactants were removed by stirring the suspension in an anhydrous ethanolic solution of 10 vol% hydrazine monohydrate. The Au-ND/BT-NT powder was obtained by repeated washing with anhydrous ethanol, acetone, and centrifugation/drying. For Au-doped samples, gold chloride hydrate was added in solution instead of Au-NDs. The resulting powders were loaded into a graphite die, and then sintered specimens were obtained using the spark plasma sintering (SPS) method. Because of possible anisotropic characteristics of TE properties of BT-based materials, thick disk-shaped polycrystalline bulk samples (10 mm diameter and 13 mm thickness) were fabricated by SPS under 30 MPa and at 360 °C for 2 min under a vacuum. Highly dense (>95% of theoretical density) polycrystalline bulk samples were obtained.

2.4. Thermoelectric measurements

The measurements for the S, σ and κ were carried out in the perpendicular direction to the SPS press direction in order to ensure the measurements of the correct TE properties. The S and σ measurements from 300 to 480 K were performed using a ULVAC ZEM-3 system. The κ values ($\kappa = \rho_s C_p \lambda$) were calculated from separated measurements: the sample density (ρ_s), the heat capacity (C_p), and the thermal diffusivity (λ), where ρ_s was determined using the dimensions and mass and λ was measured under vacuum using the laser-flash method (TC-9000, ULVAC, Japan). Low temperature (100–390 K) C_p values were collected using a Quantum Design PPMS system, and C_p was used as the constant value of 0.157 J g^{-1} K^{-1} estimated from Dulong–Petit fitting.

3. Results and discussion

3.1. Au nanoinclusion and doping

In contrast to single crystalline undoped BT, the polycrystalline stoichiometric compound BT is n-type.[27] The n-type electrical property of the present Au-ND/BT-NT composite is consistent with the nanostructured BT compounds formed from bottom-up synthesis. In this work, three different effects were demonstrated by Au addition: first, the substitutional doping of Au on the Bi site forms a point defect (Au_{Bi}^{2-}) and generates a hole. Second, the occupation of the interstitial site generates a donor with Au_i^+. Au is placed at the interstitial site between two quintets (intercalation) and achieves an electrical connection, resulting in an increase of the mobility (μ) of carriers and a reduction in κ_{latt}.[28] Recently, a few research studies about the Cu addition effects (intercalation *vs.* substitutional doping) on the TE properties of BT-based alloys including single crystals[28–30] and polycrystalline bulks[31,32] have been reported. Third, Au can be precipitated as a nanoinclusion in the matrix and/or the grain boundary region. In this case, the hetero-interface between the Au nanoinclusions and the BT-based matrix is generated. This hetero-interface might act as an energy barrier for carriers as well as an effective scattering center for phonons. In order to clarify the mechanism for ZT enhancement in this nanoinclusion-type nanocomposite, we prepared Au-ND embedded BT bulks (Au-ND/BT-NT) and evaluated their TE properties.

At a given volume content, the smaller the second phase particles are, the greater the concentration of the interface is, which could result in a simultaneous increase in phonon scattering and carrier filtering probability. However, too small-sized Au particles can rarely survive as the second phase since the melting point of Au nanoparticles drops below that of bulk Au (1337 K) when the particle radius is less than 10 nm.[33] A decrease of melting temperature in metal nanoparticles has also been reported in Ag (the melting point of ~35 nm Ag is about 350 °C).[34] Therefore, in this work, Au-NDs with a mean diameter of ~10 nm are chosen as a seed in the crystal growth of BT nanotubes. Au nanoinclusions with sizes in the range of 10–20 nm were well-dispersed in the sintered matrix and their effects on the TE properties were studied in correlation with Au-doped samples.

3.2. Microstructure and phase

We characterized the as-obtained Au-NDs, BT-NTs, and Te-NR intermediate after solution-based synthesis (Fig. 2a–d). Au-NDs were synthesized using a micro-emulsion method and used as a seed in the crystal growth of Te-NRs (Fig. 2c). Then, the Te-NRs were reacted with Bi-solution to form BT nanocrystals. Representative scanning electron microscope (SEM) images of the BT-NT (Fig. 2a and b) using Au seeds are shown. The low-resolution TEM image (Fig. 2d) of the intermediate products, Te-NR, obtained after the first step of the BT solution-based synthesis, shows the formation of uniform nanorods. A uniform distribution of a secondary phase (Au-ND) is also observed in the

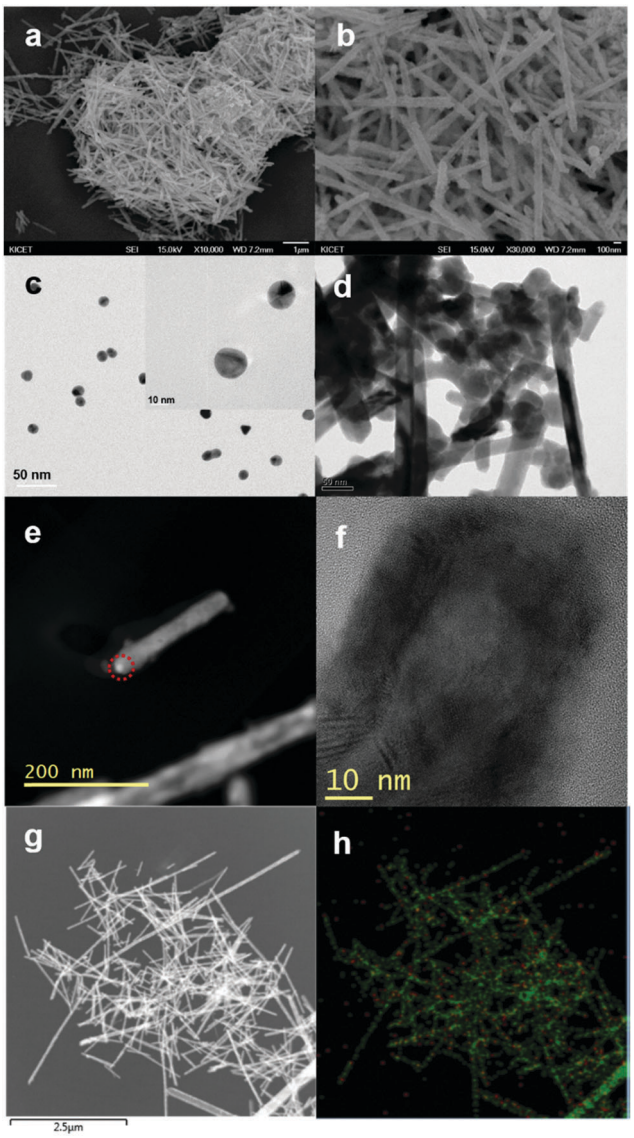

Fig. 2 (a and b) SEM image of BT-NTs. BT-NTs have a thickness of ~100 nm. (c) TEM image of Au-NDs with a diameter of ~10 nm. (d) TEM image of Te-NRs with a smaller thickness of ~20 nm. (e) STEM image of Au-ND/BT-NTs. Red circles indicate Au-NDs. (f) Tubular morphology of BT-NTs. (g and h) EDS mapping showing elemental distribution of Au (red)/Bi (green).

agglomerated BT-NTs (Fig. 2e and h). Fig. 2f shows that BT has a polycrystalline tubular morphology with a rough surface.

After the Bi alloying step, the average diameter of the BT-NTs increases to ~100 nm (Fig. 2b) from ~20 nm (Te-NR) although the size distribution is still narrow. Unlike the Te-NRs with smooth surfaces (Fig. 2d), the BT-NTs exhibit quite rough surfaces. Although Te-NRs are single crystalline (Fig. 2d), the final BT-NTs clearly exhibit polycrystalline nature with multiple crystalline domains (Fig. 2f).

Scanning transmission electron microscopy (STEM) and high-resolution transmission electron microscopy (HRTEM) images of embedded Au-NDs in the BT matrix are shown in Fig. 3a–c. This nanoinclusion is identified as Au based on the EDS analysis (Fig. 3a). According to Fig. 3b, it seems that the Au-ND size increases up to ~20 nm after the crystal growth step of Te nanorods (Te-NRs). This is possibly due to Ostwald ripening of Au-NDs as reported in CdSe–Au and Te–Au anisotropic hybrids.[35,36] Small Au-NDs on the surface of Te-NRs were dissolved to favour the growth of larger particles on Te-NRs (Fig. 1b). The migration of Au-NDs can result in preferential growth at the tip of Te-NRs since it should have higher surface energies and more accessible sites where surfactant capping is weak. Small spheres with white contrast, which is located at the tip of BT-NTs in STEM images (Fig. 2e), support the assumption. This selective growth on tips of Te-NRs could be beneficial to the uniform dispersion of Au-NDs in the thermoelectric matrix.

The HRTEM image (Fig. 3c) shows that Au-NDs with well-resolved lattice fringes are embedded in the BT matrix. The size is 10–20 nm (Fig. 3b and c), which is increased from raw Au-NDs (Fig. 2c) The selected area electron diffraction pattern is shown in Fig. 3d, confirming the embedding of single crystalline Au-NDs in the matrix.

Fig. 4a shows the typical X-ray diffraction (XRD) patterns of the Au-ND/BT-NT after solution-based synthesis, which can be readily indexed to the pure Te phase (JCPDS no. 36-1452) and the pure BT phase (JCPDS no. 15-0863). The peaks for both phases are quite broad mainly due to the finite size of our products. However, according to XRD patterns and EDS (Energy Dispersive X-ray spectroscopy) analysis, it is clear that the BT-NT after the two-step procedure is the Te-rich Bi_2Te_3 phase. Any trace of Au was not detected in XRD patterns due to the small volume fraction of Au (<1.0 vol%). By comparing the XRD patterns of sintered samples with their corresponding powders, we notice that the crystalline phase changes from Te-rich Bi_2Te_3 to pure Bi_2Te_3 and that no oxidation or secondary phase formation (except Au-NDs) occurs. There is no special preferential orientation, which means the high randomness of the BT nanograins. Fig. 4b and c indicate that all sintered samples possess a well-crystallized and void-free feature, which is consistent with their high density (>95%). As seen in Fig. 4c, the fractured surface for the bulk sample shows that nanograin structures with high aspect ratios are sintered without apparent preferential orientation for grains. The random orientation might reduce facile crack propagation along the basal plane, which is frequently observed in n-type BTS/BT ingot or pressure-sintered samples, possibly resulting in the improvement of mechanical strength. The anisotropic grains have thicknesses as small as 20–30 nm, which is smaller than BT-NT having ~100 nm thickness. This might be due to the collapse of polycrystalline BT-NTs having hollow inner space, which contributes to the reduction of κ_{latt} due to boundary phonon scattering.

3.3. Thermoelectric properties

The temperature dependence of measured S and σ of all the synthesized compositions is shown in Fig. 5a and b, respectively. Compared to pristine BT, the σ value was significantly

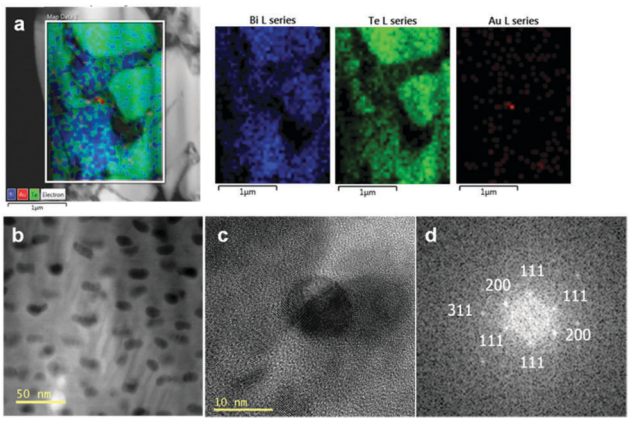

Fig. 3 (a) STEM image and EDS mapping of the Au-ND/BT-NT composite. (b) Au nanoinclusions with <20 nm diameter (dark contrast) embedded in the matrix. (c) HRTEM image of the Au-ND/BT-NT composite. Au-ND size range from 10 to 20 nm. (d) SAED patterns of Au-NDs in the BT matrix.

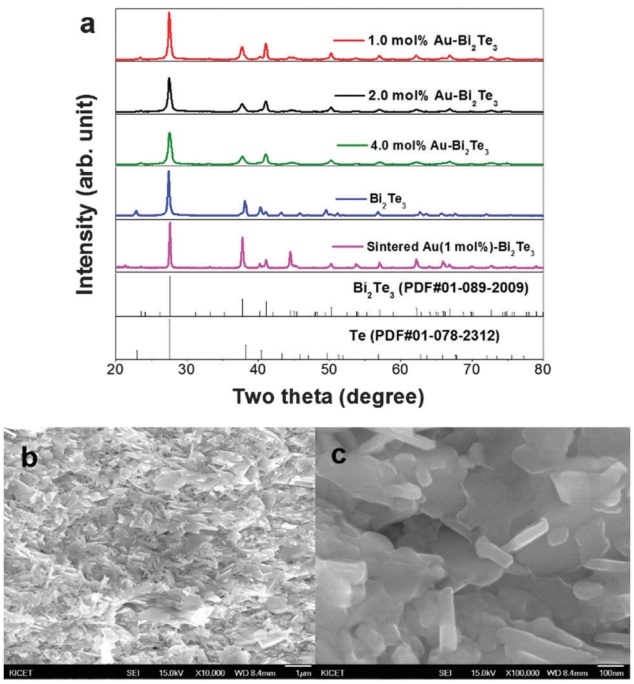

Fig. 4 (a) XRD patterns of Au-ND/BT-NT composites. (b and c) Fracture surfaces of sintered 4.0 mol% Au-ND/BT-NT composites.

increased by the introduction of 1.0 mol% Au-NDs due to electron carrier generation. This indicates that the Au could remain as NDs in the BT matrix. However, the σ values fall down with Au-ND concentration for Au-ND/BT-NT composites suggesting that some of the Au-NDs substitute Bi. During the sintering process at 360 °C, Au-NDs of size smaller than ~10 nm may be molten. Thus Au diffuses in the BT matrix and forms a point defect Au_{Bi}^{2-}, which decreases n due to the p-type doping effect. Recently, a decrease in σ by Au-doping on the Bi site has been experimentally demonstrated.[37] On the other hand, μ generally decreases with increasing Au-ND concentration due to electron scattering at the hetero-interfaces between Au-NDs and the BT matrix (Table 1).

The absolute values of S increased from −121 μV K^{-1} to −159 μV K^{-1} with an increase of Au-ND concentration from 1.0 to 5.0 mol% due to a decrease in n. However the increase in $|S|$ is rather larger considering the trade-off between S and σ. Furthermore, the temperature dependence of σ, S and power factor values for Au-ND/BT-NT samples are markedly different from Au-doped and pure BT samples. For the Au-doped samples (no nanoinclusions), $|S|$ decreases over the temperature range from 300 to 500 K. However, all Au-ND/BT-NT samples monotonically increase $|S|$ between 300 and 500 K. This is similar to the trend observed in the Cu nanoparticle decorated $Bi_{0.5}Sb_{1.5}Te_3$.[34] Therefore, the composites exhibit peak power factors and ZT values at a higher temperature than the Au-doped samples and pure BT, the feature which is more beneficial for TEG than pure BT or conventional BTS.

The overall effect on the electronic transport is elucidated in Fig. 5f, which shows the power factors for the different compositions as a function of temperature. The highest power factors

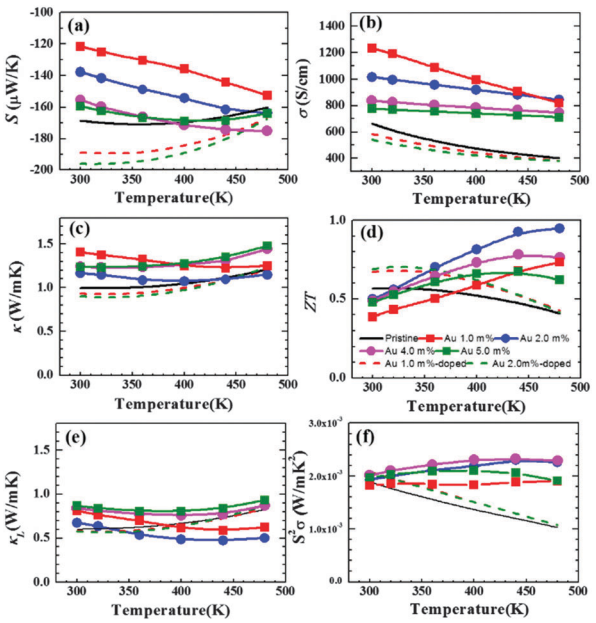

Fig. 5 Thermoelectric properties, (a) Seebeck coefficient (S), (b) electrical conductivity (σ), (c) thermal conductivity (κ), (d) figure of merit (ZT), (e) lattice thermal conductivity (κ_{latt}), and (f) power factor ($S^2\sigma$) of pristine Bi_2Te_3 (BT), Au-ND/BT-NT composites, and Au-doped samples.

Table 1 Seebeck coefficient (S), electrical conductivity (σ), mobility (μ), carrier concentration (n) at room temperature for pristine Bi_2Te_3 (BT), Au-ND/BT-NT composites (Au–BT), and Au-doped samples

Samples	S (μV K^{-1})	σ (S cm^{-1})	μ (cm^2 V^{-1} s^{-1})	n ($10^{19}cm^{-3}$)
BT	−169	664	162	2.5
1.0 mol% Au–BT	−121	1234	145	5.3
2.0 mol% Au–BT	−138	1018	135	4.7
4.0 mol% Au–BT	−155	837	119	4.4
5.0 mol% Au–BT	−159	778	113	4.3
1.0 mol% Au-doped BT	−189	586	158	2.3
2.0 mol% Au-doped BT	−196	541	159	2.1

are obtained for the 2.0 or 4.0 mol% Au-ND/BT-NT composite with a maximum value of the power factor around 450 K. Notice that in Au-ND/BT-NT composite samples, synthesized by using Au-NDs as seeds in the BT-NT growing process, the inclusion of Au-NDs (2.0 mol% Au) caused an approximately 105% increase of the electrical conductivity with only a 3% reduction of $|S|$ at 450 K. This amounts to a 92% increase in the power factor (2.3 mW m^{-1} K^{-2}) at 450 K, compared to the pristine (1.2 mW m^{-1} K^{-2}) due to improved S by a carrier filtering effect. The power factor for the Au-ND/BT-NT is larger by 27% than a maximum value of pristine at 300 K (1.8 mW m^{-1} K^{-2}).

To clarify the variation of electronic transport behavior in Au-ND/BT-NT and Au-doped samples, we calculated the density of states (DOS) effective mass m_d^* at 300 K and represented them in Fig. 6a. The m_d^* was estimated using the following equation.[9]

$$S = \frac{8\pi^2 k_B^2}{3eh^2}\left(\frac{\pi}{3n}\right)^{\frac{2}{3}} m_d^* T$$

where k_B, e, and h are the Boltzmann constant, elementary charge, and the Planck constant, respectively. Fig. 6a shows the measured S as a function of n (Pisarenko plot) at 300 K. The solid lines are calculated for m_d^* = 0.8, 1.00, and $1.2m_0$, assuming a single parabolic band and energy-independent carrier scattering approximation for degenerated semiconductors. As shown in Fig. 6a, m_d^* increases from ~$0.75m_0$ (pristine BT-NT) to ~$1.0m_0$ (2.0 mol% Au-ND/BT-NT) by Au-ND embedding. Au-doped samples also exhibit slightly increased m_d^* values compared to that for pristine BT. It is considered that larger m_d^* values for Au-ND/BT-NT and Au-doped samples are due to the modification of the electronic structure by Au-ND embedding and Au-doping[37] and could be responsible for large $|S|$. The S-n points of our Au-ND/BT-NT composites show higher positions than previously reported n-type BT-based materials as shown in Fig. 6a. Our samples shows larger m_d^* than Cu/BTS,[32] S-doped BT,[2] larger or comparable to BTS thin film with Pt nanoinclusions,[38] and BT with Bi nanoinclusions.[24]

For Au-ND/BT-NT composites, the interface between metallic Au and semiconducting BT might induce an energy dependent carrier scattering effect by introducing a well defined energy barrier which filters the carrier with small energy. When Φ of metal is larger than that of BT, V_B is approximately Φ (metal) $-\Phi$(BT) (upper panel of Fig. 6b). Pt has a higher work function (5.65 eV)[38] than Au and therefore the potential barrier, V_B, for the Pt/BT interface (V_B ~ 0.25 eV) should be larger than that for Au/BT

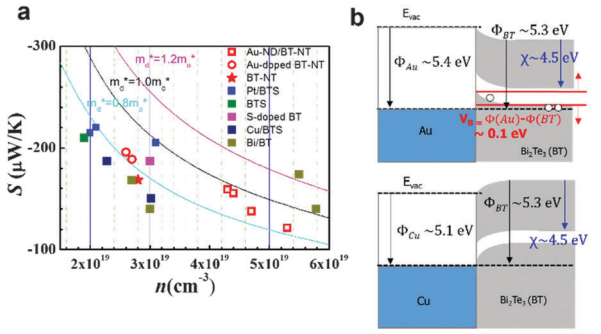

Fig. 6 (a) Seebeck coefficient (S) as a function of carrier concentration (n) for Au-ND/BT-NTs, Au-doped BT-NTs, and pristine BT-NTs. The S values are compared with reported values of Pt/BTS (ref. 38), Bi/BTS (ref. 24), Cu/BTS (ref. 32), and S-doped BT (ref. 2). (b) Simple band diagram for Au/BT (upper) and Cu/BT (lower). For the Cu/BT interface, no potential barrier for energy filtering is formed.

($V_B \sim 0.1$ eV). A potential barrier of around 0.1 eV is predicted to be optimal in the power factor enhancement according to the previous study.[5,15] When metal with smaller Φ than BT is involved, the formation of a potential barrier is dependent on situation. When Cu is included in the BT matrix, the energy filtering effect is not evident,[32] which can be attributed to the absence of V_B due to work function of Cu (4.5–5.1 eV) as shown in Fig. 6b. On the other hand, as for the Bi/BT interface, Φ of Bi is smaller (4.3 eV) than that of BT, V_B is approximately χ (BT) $-\Phi$ (Bi). The potential barrier, V_B, for the Bi/BT interface is approximately 0.2 eV, which could be effective in the S enhancement.[24] Recently, similar results were also experimentally demonstrated in p-type Sb_2Te_3 by introduction of nano-scale Pt or AgTe.[39,40] The present material design concept for S enhancement by the carrier filtering effect would be generally applicable to other TE materials.

Fig. 5c and e a shows κ and κ_{latt} of bulk BT samples with different content of Au-NDs as a function of temperature. Since the κ consists of electronic thermal conductivity ($\kappa_{ele} = \kappa - \kappa_{latt}$), κ_{latt}, and bipolar thermal conductivity (κ_{bp}), and κ_{bp} is usually negligible near room temperature, κ_{latt} is therefore obtained by directly subtracting κ_{ele} from κ. However, in the Au-doped BT system, the bipolar terms cannot be excluded in high temperature (>350 K) as shown in Fig. 5c and e, which is in contrast with Au-ND/BT-NT. Based on the Wiedemann–Franz law, κ_{ele} is roughly calculated by the relation $\kappa_{ele} = L\sigma T$, where the L value, the Lorentz number, at 300 K, was assumed to be 2.0×10^{-8} V^2 K^{-2} for BT and Au-ND/BT-NT.[41–43] As shown in Fig. 5c and e, the dispersion of Au-NDs significantly reduces κ_{latt} especially in the high temperature range. The minimum value reaches as low as 0.47 W m^{-1} K^{-1} for bulk BT with 2.0 mol% Au-NDs at 450 K, which is much lower than that of pristine bulk BT (0.73 W m^{-1} K^{-1}). The reduction in κ_{latt} is thought to be caused by strong scattering of phonons in the presence of Au-NDs. Considering the size of dispersed Au-NDs (10–20 nm), phonons with short and medium mean free paths (3–100 nm) were effectively scattered by Au-NDs. However, κ_{latt} values for the materials at high Au contents (4.0 and 5.0 mol%) are rather higher even at high temperatures. This is considered to be related with the high κ of Au (~ 320 W m^{-1} K^{-1} at 300 K). A similar result has been reported in the Te (~ 3 W m^{-1} K^{-1} at 300 K) nanoparticle embedded p-type $Bi_{0.5}Sb_{1.5}Te_3$ thin film.[23]

The dimensionless TE figures of merit ZT of all bulk samples are calculated and the results are shown in Fig. 5d. It is found that the ZT values for all Au-ND/BT-NT composites increase with increasing temperature, which is different from the variation trend of single-phase bulk BT. Furthermore, the dispersion of Au-NDs leads to a remarkable increase in ZT, reaching a maximum ZT value of 0.95 at 480 K from the bulk BT dispersed with 2.0 mol% Au-ND, approximately 67% higher than that of the BT matrix. The results indicate that the dispersion of Au-NDs can lead to a significant enhancement of TE performance for BT-based materials over the whole temperature range given that the Au-NP content is controlled properly. In this work, the improvement in ZT of Au-ND dispersed BT is mainly attributed to two factors: (i) creation of barrier potential in the interface between two phases, due to a different Φ between Au-NDs and the BT matrix, and therefore scattering low-energy electrons to improve S and (ii) reduced κ_{latt} due to newly formed interfaces/boundaries, nanoscale precipitates, and point-defect scattering, causing phonon scattering.

Conclusions

We have successfully demonstrated that Au nanodot embedded Bi_2Te_3 composites with enhanced thermoelectric properties can be synthesized through bottom-up synthesis and consolidation by spark plasma sintering. The introduction of a small amount of Au nanodots effectively increased the power factor due to the carrier filtering effect. Additionally, they decreased lattice thermal conductivity by intensified phonon scattering at the highly dense phase boundary between Au and Bi_2Te_3. A maximum ZT value of 0.95 was obtained at 480 K in 2.0 mol% Au nanodot embedded Bi_2Te_3, which is approximately 67% higher than that of the pristine BT. Au nanodots simultaneously modulate the electronic and thermal transport behaviour of n-type Bi_2Te_3-based materials.

Acknowledgements

This study was supported by 2015 Research Grant from Kangwon National University (No. 520150035), the National Research Foundation of Korea (NRF) Grant funded by the Korean Government (MSIP) (No. 2015R1A5A1037668), the Basic Science Research Program through the NRF funded by the Ministry of Education (No. 2015R1D1A3A01018534), and the Fundamental R&D program for Core Technology of Materials funded by the Ministry of Knowledge Economy, Republic of Korea (10048035).

Notes and references

1 Y. Zhang, G. Xu, J. Mi, F. Han, Z. Wang and C. Ge, *Mater. Res. Bull.*, 2011, **45**, 760.
2 R. J. Mehta, Y. Zhang, C. Karthik, B. Singh, R. W. Siegel, T. Borca-Tasciuc and G. Ramanath, *Nat. Mater.*, 2011, **11**, 233.

3 J. S. Son, M. K. Choi, M. K. Han, K. Park, J. Y. Kim, S. J. Lim, M. Oh, Y. Kuk, C. Park, S. J. Kim and T. Hyeon, *Nano Lett.*, 2012, **12**, 640.
4 Y. Min, J. W. Roh, H. Yang, M. Park, S. I. Kim, S. Hwang, S. M. Lee, K. H. Lee and U. Jeong, *Adv. Mater.*, 2013, **25**, 1425.
5 S. V. Faleev and F. Leonard, *Phys. Rev. B: Condens. Matter Mater. Phys.*, 2008, **77**, 214304.
6 M. Zebarjadi, K. Esfarjani, A. Shakouri, J.-H. Bahk, Z. Bian, G. Zeng, J. Bowers, H. Lu, J. Zide and A. Gossard, *Appl. Phys. Lett.*, 2009, **94**, 202105.
7 M. G. Kanatzidis, *Chem. Mater.*, 2010, **22**, 648.
8 A. J. Minnich, M. S. Dresselhaus, Z. F. Ren and G. Chen, *Energy Environ. Sci.*, 2009, **2**, 466.
9 G. J. Snyder and E. S. Toberer, *Nat. Mater.*, 2008, **7**, 105.
10 D. L. Medlin and G. J. Snyder, *Curr. Opin. Colloid Interface Sci.*, 2009, **14**, 226.
11 B. Moyzhes and V. Nemchinsky, *Appl. Phys. Lett.*, 1998, **73**, 1895.
12 Y. Nishio and T. Hirano, *Jpn. J. Appl. Phys.*, 1997, **36**, 170.
13 D. Vashaee and A. Shakouri, *Phys. Rev. Lett.*, 2004, **92**, 106103.
14 J. M. O. Zide, D. Vashaee, Z. X. Bian, G. Zeng, J. E. Bowers, A. Shakouri and A. C. Gossard, *Phys. Rev. B: Condens. Matter Mater. Phys.*, 2006, **74**, 205335.
15 A. Popescu, L. M. Woods, J. Martin and G. S. Nolas, *Phys. Rev. B: Condens. Matter Mater. Phys.*, 2009, **79**, 205302.
16 J. P. Heremans, C. M. Thrush and D. T. Morelli, *Phys. Rev. B: Condens. Matter Mater. Phys.*, 2004, **70**, 115334.
17 J. P. Heremans, C. M. Thrush and D. T. Morelli, *J. Appl. Phys.*, 2005, **98**, 063703.
18 J. M. O. Zide, J.-H. Bahk, R. Singh, M. Zebarjadi, G. Zeng, H. Lu, J. P. Feser, D. Xu, S. L. Singer, Z. X. Bian, A. Majumdar, J. E. Bowers, A. Shakouri and A. C. Gossard, *J. Appl. Phys.*, 2010, **108**, 123702.
19 J. Martin, L. Wang, L. Chen and G. S. Nolas, *Phys. Rev. B: Condens. Matter Mater. Phys.*, 2009, **79**, 115311.
20 B. Paul and P. Banerji, *J. Appl. Phys.*, 2010, **108**, 064322.
21 J. R. Sootsman, H. Kong, C. Uher, J. J. D'Angelo, C.-I. Wu, T. P. Hogan, T. Caillat and M. G. Kanatzidis, *Angew. Chem., Int. Ed.*, 2008, **47**, 8618.
22 H. L. Skriver and N. M. Rosengaard, *Phys. Rev. B: Condens. Matter Mater. Phys.*, 1992, **46**, 7157.
23 S. I. Kim, S. Hwang, J. W. Roh, K. Ahn, D.-H. Yeon and K. H. Lee, *J. Mater. Res.*, 2012, **27**, 2449.
24 S. Sumithra, N. J. Takas, D. K. Misra, W. M. Nolting, P. F. P. Poudeu and K. L. Stokes, *Adv. Energy Mater.*, 2011, **1**, 1141.
25 D. Haneman, *J. Phys. Chem. Solids*, 1959, **11**, 205.
26 M. Chen, J.-P. Peng, H.-M. Zhang, L.-L. Wang, K. He, X.-C. Ma and Q.-K. Xue, *Appl. Phys. Lett.*, 2012, **101**, 081603.
27 J. P. Fleurial, L. Gailliard, R. Triboulet, H. Scherrer and S. Scherrer, *J. Phys. Chem. Solids*, 1988, **49**, 1237.
28 T. Svechnikova, P. Konstatinov and G. Alekseeva, *Inorg. Mater.*, 2000, **36**, 556.
29 T. McCarthy and H. Goldsmid, *J. Phys. D: Appl. Phys.*, 1970, **3**, 697.
30 J. Bludska, S. Karamazov, J. Navratil, I. Jakubec and J. Horak, *Solid State Ionics*, 2004, **171**, 251.
31 J. Cui, L. Mao, W. Yang, X. Xu, D. Chen and W. Xiu, *J. Solid State Chem.*, 2007, **180**, 3583.
32 W. Liu, Q. Zhang, Y. Lan, S. Chen, X. Yan, Q. Zhang, H. Wang, D. Wang, G. Chen and Z. Ren, *Adv. Energy Mater.*, 2011, **1**, 577.
33 P. H. Buffat and J.-P. Borel, *Phys. Rev. A: At., Mol., Opt. Phys.*, 1975, **13**, 2287.
34 K. H. Lee, H. S. Kim, S. I. Kim, E. S. Lee, S. M. Lee, J. S. Rhyee, J. Y. Jung, I. H. Kim, Y. Wang and K. Koumoto, *J. Electron. Mater.*, 2012, **41**, 1165.
35 T. Mokari, E. Rothenberg, I. Popov, R. Costi and U. Banin, *Science*, 2004, **304**, 1787.
36 T. P. Vinod, M. Yang, J. Kim and N. A. Kotov, *Langmuir*, 2009, **25**, 13545.
37 K. H. Lee, S. I. Kim, H. Mun, B. Ryu, S. M. Choi, H. J. Park, S. Hwang and S. W. Kim, *J. Mater. Chem. C*, 2015, **3**, 10604.
38 T. Sun, M. K. Samani, N. Khosravian, K. M. Ang, Q. Yan, B. K. Tay and H. H. Hng, *Nano Energy*, 2014, **8**, 223.
39 D.-K. Ko, Y. Kang and C. B. Murray, *Nano Lett.*, 2011, **11**, 2841.
40 Y. Zhang, M. L. Snedaker, C. S. Birkel, S. Mubeen, X. Ji, Y. Shi, D. Liu, X. Liu, M. Moskovits and G. D. Stucky, *Nano Lett.*, 2011, **12**, 1075.
41 L. Zhao, S. Lo, J. He, H. Li, K. Biswas, J. Androulakis, C. Wu, T. P. Hogan, D. Chung, V. P. Dravid and M. G. Kanatzidis, *J. Am. Chem. Soc.*, 2011, **133**, 20476.
42 K. T. Wojciechowski and M. Schmidt, *Phys. Rev. B: Condens. Matter Mater. Phys.*, 2009, **79**, 184202.
43 L. D. Zhao, J. Q. He, C. I. Wu, T. P. Hogan, X. Y. Zhou, C. Uher, V. P. Dravid and M. G. Kanatzidis, *J. Am. Chem. Soc.*, 2012, **134**, 7902.